A Spatial Parallel Kinematic Manipulator with Nested Kinematic Chains and High Rotational Range

Wesley Emile Dharmalingum * and Jared Padayachee

Discipline of Mechanical Engineering, University of KwaZulu-Natal, Durban, South Africa;
Email: padayacheej@ukzn.ac.za (J.P.)
*Correspondence: dharmalingumw@ukzn.ac.za (W.E.D.)

***Abstract*—The paper presents the design and development of a novel five Degree of Freedom (DOF) Parallel Kinematic Manipulator (PKM) which possesses 3 pairs of coplanar limbs with nested kinematic chains. The design employs actuated prismatic joints and passive revolute joints. Universal joints were decoupled into individual revolute joints to achieve a high rotational range of the end effector about two axes. A pair of coplanar limbs exhibited either a Parallelogram (Pa) or an Irregular Quadrilateral (IQ) structure which was dependent on the orientation of the end effector. The PKM, named the 2-R (Pa-IQ) RR, R(Pa-IQ) R manipulator, possesses three translational DOFs, two rotational DOFs and a parasitic rotational DOF. The inverse kinematic analysis was solved by applying the vector method twice. SolidWorks® and MATLAB® simulations were used to validate the inverse kinematic equations. The Monte Carlo method was used to generate the workspace volume. An additive manufactured desktop prototype was developed and used for testing and experimentation.**

***Keywords*—parallel kinematic manipulator, rotation, kinematics, workspace**

I. Introduction

Parallel Kinematic Manipulators (PKMs) have attracted significant attention in recent years. A PKM possesses two or more closed kinematic loops with each limb connected to the base and end effector [1]. PKMs are suitable for fine positioning applications, packaging assembly lines, part handling, motion simulation, medical operations and as micro-robots. Concerning stiffness and rigidity, PKMs perform better than serial manipulators. Due to the attachment of multiple limbs to the end effector and base, PKMs inherently possess a high payload to weight ratio. One of the drawbacks of PKMs is the relatively small workspace, limited rotational range, and complex forward kinematic analysis and calibration procedures [2].

PKMs exhibit limited rotation of the end effector due to mechanical interference between components. Rotation limits are also attributed to individual joint limits. Researchers have investigated methods to increase the rotational performance of PKMs by exploiting the arrangement of joints, architectural layout and by designing hybrid robotic platforms. Lui *et al.* [3] proposed a new family of three Degree of Freedom (DOF) PKMs with high rotational range. The PKMs possessed three non-identical limbs with at least one limb containing a planar four-bar parallelogram joint. The use of single DOF joints ensured that the family of PKMs were capable of high rotational range. One 3-DOF PKM design achieved a range of ±45°. Researchers have explored the concept of exploiting 1-DOF joints by implementing orthogonal non-intersecting revolute joints as an alternative to the traditional universal joint on 6-DOF PKMs. The revolute joints offered better manufacturability, fewer geometric constraints, improved stiffness and larger workspaces could be generated. The kinematic analysis required novel methodologies to treat the offset revolute joints [4, 5].

Oh *et al.* [6, 7] developed a 3-DOF micro PKM suitable for positioning applications. The PKM achieved a tilt range of 100° and implemented a dual stage system. A family of 3-DOF PKMs was sythesised by Jin *et al.* [8] based on the crank-and-rocker mechanism. Some of the presented PKMs could achieve reachable tilt angles larger than 180°. Such PKMs with large reachable tilt angles were suited for fast and low accuracy applications. Staicu *et al.* [9] developed a high-speed pick-and-place 4-DOF PKM with four identical limbs. Parallelogram joints, simple links and a unique end effector were used. The PKM was able to achive a ±90° rotation about its vertical axis. Liu *et al.* [10] developed a 5-DOF PKM for flexible 5-axis machining of large structural components and to perform remote maintenance. The PKM had a tilt angle reach and swing capacity of 30° and 110° respectively and possessed non-identical limbs placed onto a dome-shaped base. Xialong *et al.* [11] implemented actuation redundancy to develop a 5-DOF PKM with non-identical limbs. The PKM was able to achieve three rotations and two translations. The range of rotational motion about each axis was ±30°. The 5-DOF Metrom Pentapod was developed to perform machining applications with its end effector able to reach rotation ranges of ±90° about two axes. The unique attachment of the limbs to the end

Manuscript received March 17, 2023; revised April 30, 2023; accepted May 30, 2023.

effector aided the high rotational capability which also used two revolute joints as a substitute to a universal joint concerning the limb attachment scheme to the end effector. However, the PKM still implemented spherical joints to attach the limbs to the base [12].

Sun *et al.* [13] used the concept of hybridisation to develop the 5 DOF T5PKM, which integrated two parallel kinematic structures. The hybrid layout allowed the end effector to achieve up to 30 °rotations about two axes. An extensive review of PKMs conducted by Weck and Staimer *et al.* [12] showed that hybrid robotic platforms that use a PKM layout can generally achieve large rotational range with some architectures exceeding 100 ° rotations. The drawback is the complex kinematic analysis of hybrid PKMs, leading to further difficulty in control and stabilization [14].

Researchers have also investigated the design of PKMs whose end effector possess an unlimited rotation. Kiselev *et al.* [15] presented families of PKMs with a circular guide that possessed an unlimited rotation about one axis. Qazani *et al.* [16] exploited axisymmetric design to produce a novel 6-DOF PKM called the Hexarot manipulator. The manipulator possessed six coaxial actuated arms. Gosselin *et al.* [17] developed a singularity-free kinematically redundant PRR planar PKM with an unlimited rotation about one axis. Schreiber and Gosselin also used kinematic redundancy to develop the SPARA PKM with Schönflies Motion and unlimited end effector rotation within a large translation workspace [18].

This research exclusively utilised 1-DOF joints, actuated parallelogram joints and orthogonal non-intersecting revolute joints instead of universal joints to realise high ranges of rotation. The concept of actuated parallelogram joints has not been explored in literature and it is addressed in this paper. Section I of the paper introduces the research and provides a context for the study. Section II presents the machine topology. Section III presents the inverse kinematic analysis. Section IV and V presents the results from simulations and experimentation respectively. Section VI provides a conclusion to the paper.

II. Machine Topology

The Grübler Kutzbach equation was applied to the mechanism and the calculation is presented in Eq. (1). The PKM comprised of 28 links which represents the value for n. There exists 20 binary joints and 6 ternary joints therefore j = 32. This PKM is classified as a spatial PKM therefore λ = 6. The sum of all the joint freedoms, f_i, is 26 since there are 6 prismatic and 20 revolute joints.

$$F = \lambda(n - j - 1) + \Sigma f_i \tag{1}$$

$$F = 6(28 - 32 - 1) + 26 = -4$$

The negative value of −4 indicated that the PKM is an over-constrained mechanism [19]. Over-constrained mechanisms have the potential to increase rigidity which is a result of the end effector losing one or more DOFs or permitting one or more DOFs as parasitic movements. The number of DOFs of the PKM was confirmed through simulations and physical testing as presented in Section III, IV and V. The PKM is redundantly actuated since there are 6 actuators and 5 independent DOFs. The drawbacks of redundantly actuated PKMs are that there exist motion constraint equations and there can be an infinite number of solutions to the inverse dynamic problem. Some advantages that a redundantly actuated PKM possesses are the potential of a singularity free workspace and the generation of larger force magnitudes [20].

The PKM is comprised of three pairs of limbs namely limb pairs 1–2, 3–4 and 5–6. The limbs are connected to the base and end effector by revolute joints. Within each limb is an actuated prismatic joint. Limb 5 and 6 are rotated at 90 °relative to the arrangement of limb pairs 1–2 and 3–4. Limb 5 and 6 are side-by-side with one less revolute joint which classifies the limbs of the PKM as non-identical limbs. The angles μ and ϕ, shown in Fig. 5, are 42.93 °and 47.07 °respectively which is dependent on the machine geometric parameters shown in Table I. The robotic architecture is capable of independent translation along the x, y and z axes and independent rotations about the x and y axes. However, the PKM possesses a parasitic rotation about the z axis. Rotation about the z axis is dependent on the rotations about the x and y axes. When the end effector exhibits translational motion, the nested kinematic loops exhibit a Parallelogram (Pa) structure. When the end effector exhibits rotational movement, at least one of the nested kinematic loops exhibits an Irregular Quadrilateral (IQ) structure therefore the PKM was named the 2-R(Pa-IQ) RR, R(Pa-IQ) R Parallel Manipulator. Fig. 1 depicts the topology of the PKM.

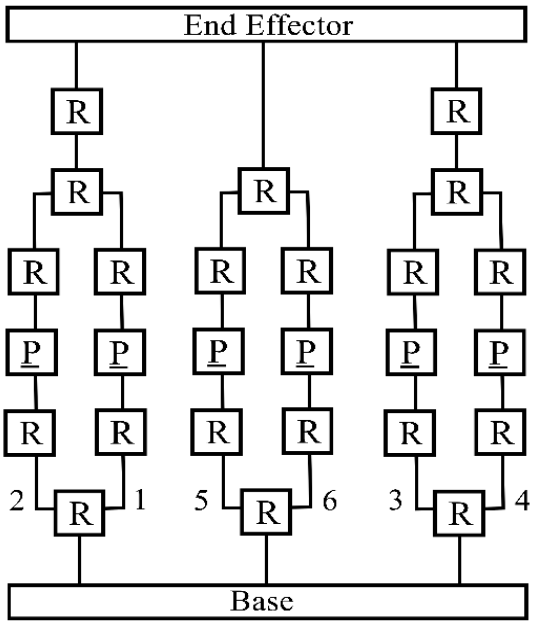

Figure 1. Machine topology.

The geometric parameters of the PKM shown in Fig. 2 are documented in Table I. The dimensions were selected based on the available additive manufacturing equipment.

TABLE I. GEOMETRIC PARAMETERS

Variable	Value (mm)
$OA_{1,2} = OA_{3,4}$	150
$OA_{5,6}$	161.55
$A_{1,2}B_1 = A_{3,4}B_3$	104.92
$A_{1,2}B_2 = A_{3,4}B_4$	170.14
$C_1D_{1,2} = C_3D_{3,4}$	58.73
$C_2D_{1,2} = C_4D_{3,4}$	74.63
$PD_{1,2} = PD_{3,4}$	38.69
$PD_5 = PD_6$	46.06
$A_{1,2}A_{3,4}$	259.81
$A_{1,2}A_{5,6} = A_{3,4}A_{5,6}$	266.65
$D_{1,2}D_{3,4}$	58.65
$D_{1,2}D_5 = D_{3,4}D_6$ 6	67.01
$B_1B_2 = C_1C_2$	82.46
D_5D_6	50.00
Length of actuator when fully retracted	$A_{1,2}D_{1,2} = A_{3,4}D_{3,4}$ = 184 $A_5D_5 = A_6D_6$ = 192
Length of actuator when fully extended	$A_{1,2}D_{1,2} = A_{3,4}D_{3,4}$ = 250 $A_5D_5 = A_6D_6$ = 258

III. INVERSE KINEMATIC ANALYSIS

A. Outer Vector Loop Analysis

Additional analytical considerations must be accounted for to treat the complexity introduced by orthogonal non-intersecting revolute joints [4, 5]. Vector loops were applied twice to each limb to generate the inverse kinematic equations. This approach formed inner and outer vector loops which accommodated the offset revolute joints and actuated parallelogram joints. Fig. 2 illustrates the outer vector loop in green which is constructed from four vectors involving points O, A, P, and D. Point O lies on the base link and is coincident with the origin of the global coordinate system. Point A lies on the base and is coincident with the axis of rotation of the revolute joints on the base. Point P is a reference point on the mid-point of the end effector and is coincident with the origin of a local coordinate system placed on the end effector. Point D is a reference point on the axis of the revolute joints on the end effector. The outer vector loop equations were developed to calculate the magnitude of vector $\overrightarrow{AD}$. The rotation matrix was applied to vector $\overrightarrow{PD}$ to allow the vector to be defined with respect to the global coordinate system. The inverse kinematic analysis accommodated for translation, α rotation with translation and β rotation with translation. As a result, the equations did not address the parasitic rotation and the rotation matrix was simplified as shown in Eq. (4). The parasitic rotation will be addressed in future work.

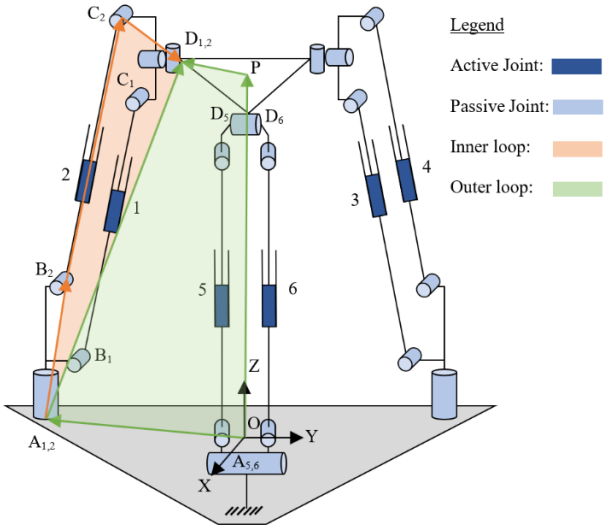

Figure 2. The inner and outer vector loops.

The outer vector loop equation for limb 1 and 2 is presented and expanded as shown in Eqs. (2)–(5).

$$\overrightarrow{OA_{1,2}} + \overrightarrow{A_{1,2}D_{1,2}} = \overrightarrow{OP} + R(\beta,\alpha)\overrightarrow{PD_{1,2}} \quad (2)$$

$$J = K \quad (3)$$

where J and K represents Eqs. (4) and (5) respectively. Also, c and s represents cosine and sine respectively.

$$J = \begin{bmatrix} (\overrightarrow{OA_{1,2}})_x \\ (\overrightarrow{OA_{1,2}})_y \\ (\overrightarrow{OA_{1,2}})_z \end{bmatrix} + \begin{bmatrix} (\overrightarrow{A_{1,2}D_{1,2}})_x \\ (\overrightarrow{A_{1,2}D_{1,2}})_y \\ (\overrightarrow{A_{1,2}D_{1,2}})_z \end{bmatrix} \quad (4)$$

$$K = \begin{bmatrix} (\overrightarrow{OP})_x \\ (\overrightarrow{OP})_y \\ (\overrightarrow{OP})_z \end{bmatrix} + \begin{bmatrix} c\beta & s\beta s\alpha & s\beta c\alpha \\ 0 & c\alpha & -s\alpha \\ -s\beta & c\beta s\alpha & c\beta c\alpha \end{bmatrix} \begin{bmatrix} (\overrightarrow{PD_{1,2}})_x \\ (\overrightarrow{PD_{1,2}})_y \\ (\overrightarrow{PD_{1,2}})_z \end{bmatrix} \quad (5)$$

Let L, M and N represent the first, second and third rows respectively concerning the expanded form of Eq. (5) with vector $\overrightarrow{A_{1,2}D_{1,2}}$ on the left-hand side of the equation. The magnitude of vector $\overrightarrow{A_{1,2}D_{1,2}}$ is calculated in Eq. (6).

$$\left|\overrightarrow{A_{1,2}D_{1,2}}\right| = \begin{vmatrix} (\overrightarrow{A_{1,2}D_{1,2}})_x \\ (\overrightarrow{A_{1,2}D_{1,2}})_y \\ (\overrightarrow{A_{1,2}D_{1,2}})_z \end{vmatrix} = \sqrt{L^2 + M^2 + N^2} \quad (6)$$

B. Inner Vector Loop Analysis

The inner vector loop for limb 2 is shown in Fig. 2 by the orange vectors and vector $\overrightarrow{AD}$ from the outer loop. The inner vector loop analysis was treated as a 2-dimensional analysis due to the actuated parallelogram limb arrangement constraining a pair of limbs along a plane. Vector $\overrightarrow{AB}$ and vector $\overrightarrow{CD}$ are machine design parameters, therefore, the only unknown in the inner vector loop is vector $\overrightarrow{B_2C_2}$ which represents the length of the linear

actuator. The inner vector loop equation for limb 1 and 2 is described by Eq. (7).

$$\overrightarrow{B_iC_i} = \overrightarrow{A_{1,2}D_{1,2}} - \overrightarrow{A_{1,2}B_i} - \overrightarrow{C_iD_{1,2}} \quad (7)$$

where i = 1 or 2.

With the inner vector loop analysis conducted as a 2-dimensional analysis, vector $\overrightarrow{AD}$ needed to be treated to describe its 2-dimensional representation since it was solved as a 3-dimensional vector from the outer vector loop analysis. Fig. 3 shows a local coordinate system placed at point A to establish a x-z plane. The y component from vector $\overrightarrow{AD}$ was set to zero without losing vector integrity and to allow the vector to be converted to a 2-dimensional vector. The z component of vector $\overrightarrow{AD}$ was retained from the outer vector loop analysis. The new x component of vector $\overrightarrow{AD}$ was calculated using the theorem of Pythagoras. This method was applied to limb 3 and 4 as they are identical in composition and layout to limb 1 and 2.

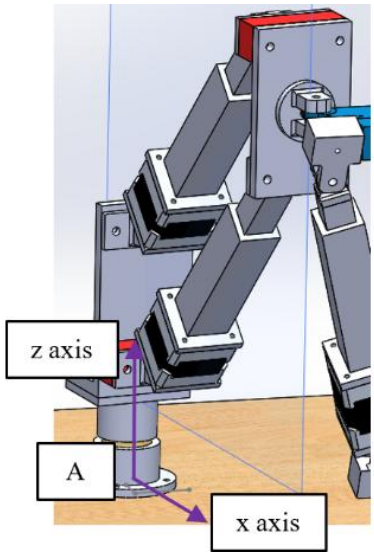

Figure 3. The 2-dimensional plane of the actuated parallelogram joint for limb 1 and 2.

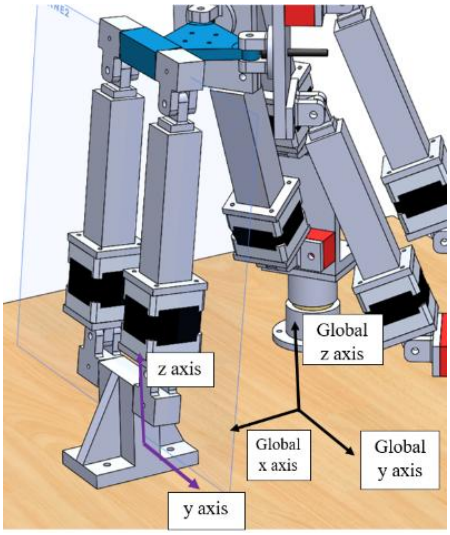

Figure 4. The 2-dimensional plane of the actuated parallelogram joint for limb 5 and 6.

Concerning limb 5 and 6, the y value was retained from the outer loop analysis for vector $\overrightarrow{AD}$ and the x value was set to zero. Fig. 4 shows that a local coordinate system was established at the base for limb 5 and 6. The pair of limbs are constrained to move along the plane shown in Fig. 4 which also moves in space. A new z value was computed for limb 5 and 6 using the theorem of Pythagoras. Limb 5 and 6 were treated differently in comparison to the other limb pairs due to its different orientation.

Eq. (7) is expanded and described by Eq. (8).

$$\begin{bmatrix} (\overrightarrow{B_iC_i})_x \\ (\overrightarrow{B_iC_i})_y \\ (\overrightarrow{B_iC_i})_z \end{bmatrix} = \begin{bmatrix} (\overrightarrow{A_{1,2}D_{1,2}})_x \\ (\overrightarrow{A_{1,2}D_{1,2}})_y \\ (\overrightarrow{A_{1,2}D_{1,2}})_z \end{bmatrix} - \begin{bmatrix} (\overrightarrow{A_{1,2}B_i})_x \\ (\overrightarrow{A_{1,2}B_i})_y \\ (\overrightarrow{A_{1,2}B_i})_z \end{bmatrix} - \begin{bmatrix} (\overrightarrow{C_iD_{1,2}})_x \\ (\overrightarrow{C_iD_{1,2}})_y \\ (\overrightarrow{C_iD_{1,2}})_z \end{bmatrix} \quad (8)$$

The x component of vector $\overrightarrow{A_{1,2}D_{1,2}}$ is calculated using Eq. (9).

$$(\overrightarrow{A_{1,2}D_{1,2}})_x = \sqrt{|\overrightarrow{A_{1,2}D_{1,2}}|^2 - (\overrightarrow{A_{1,2}D_{1,2}})_z^2} \quad (9)$$

Let Q and R represent the first and third rows respectively of the right-hand side of Eq. (8). The magnitude of vector $\overrightarrow{B_iC_i}$ is determined by Eq. (10).

$$|\overrightarrow{B_iC_i}| = \begin{vmatrix} (\overrightarrow{B_iC_i})_x \\ 0 \\ (\overrightarrow{B_iC_i})_z \end{vmatrix} = \sqrt{Q^2 + R^2} \quad (10)$$

When the end effector rotates, the components of vector $\overrightarrow{C_iD_{1,2}}$ change as shown in Fig. 5. The angles μ and ϕ shown in Fig. 5, are a result of the design parameters of the prototype. The gradient of the line $E_{1,2}F_{1,2}$ is equal to the gradient of the line $(\overrightarrow{C_iD_{1,2}})_z$. This aided in the calculation of angle ϕ and ψ_1.

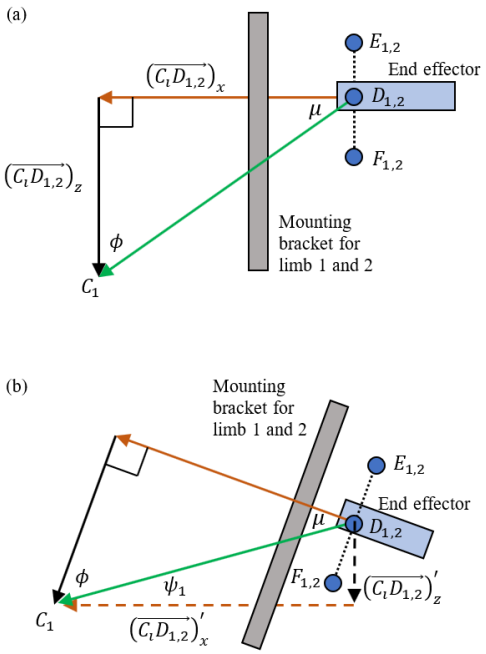

Figure 5. Changes in vector CD during rotation of the end effector. (a) Mounting bracket position for 0 ° rotation of the end effector. (b) Mounting bracket leaning forward after a rotation of the end effector.

The new components of the $\overrightarrow{C_iD_{1,2}}$ vector concerning limb 1 is given by Eq. (11) and Eq. (12).

$$\left(\overrightarrow{C_iD_{1,2}}\right)'_x = \left|\overrightarrow{C_iD_{1,2}}\right|(\cos\psi_1) \quad (11)$$

$$\left(\overrightarrow{C_iD_{1,2}}\right)'_z = \left|\overrightarrow{C_iD_{1,2}}\right|(\sin\psi_1) \quad (12)$$

The vectors $\left(\overrightarrow{C_iD_{1,2}}\right)'_x$ and $\left(\overrightarrow{C_iD_{1,2}}\right)'_z$ replace $\left(\overrightarrow{C_iD_{1,2}}\right)_x$ and $\left(\overrightarrow{C_iD_{1,2}}\right)_z$ respectively in Eq. (8) when rotation occurs.

IV. Simulation Results

A. Workspace

The workspace was generated using the Monte Carlo method, which has been successfully implemented by researchers in [21–23]. The Monte Carlo method was used in conjunction with the inverse kinematic solution. Random coordinates and rotation angles were generated within an upper and lower limit. Points that satisfied the actuation limits and the PKM mechanical constraints were plotted forming a point cloud. The convex hull boundary wrapping method was performed on MATLAB® to obtain the wrapped volume, thereby providing the workspace for the PKM. The Monte Carlo method was best suited for the workspace analysis due to the architectural complexity and unintuitive workspace.

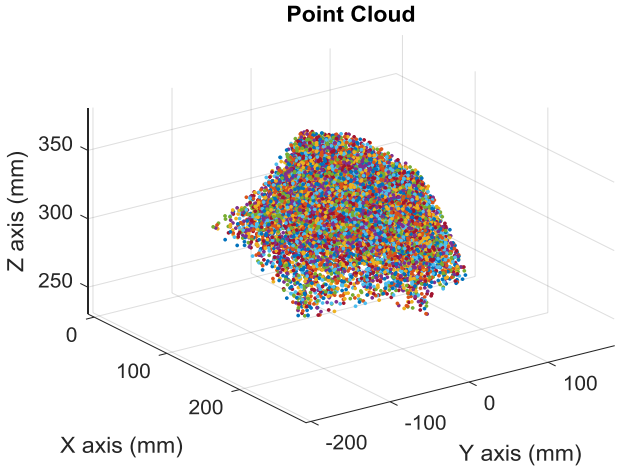

Figure 6. Workspace point cloud for constant orientation at 0 °.

The constant orientation workspace point cloud is shown in Fig. 6 and the convex hull wrapping is depicted in Fig. 7. Fig 8. shows the distribution of the 12000 points that constitute the point cloud. The center of the point cloud was more densely populated as indicated by the individual heights of the bars and the colour bar. The coordinates of the end effector, in terms of x, y and z, at full retraction was (87.82; 0; 295.83). The workspace boundary under the constant orientation conditions is detailed in Table II.

TABLE II. Summary of the Workspace Boundary for Constant Orientation

Axes	Value (mm)	Reason for limitation
x minimum	46.50	Self-clashing
x maximum	235.14	Maximum stroke length of actuator 1–4.
y minimum	136.12	Maximum stroke length of actuator 3 and 4.
y maximum	−136.12	Maximum stroke length of actuator 1 and 2.
z minimum	262.08	Maximum stroke length for actuator 1–4.
z maximum	356.68	Maximum stroke length of actuators.

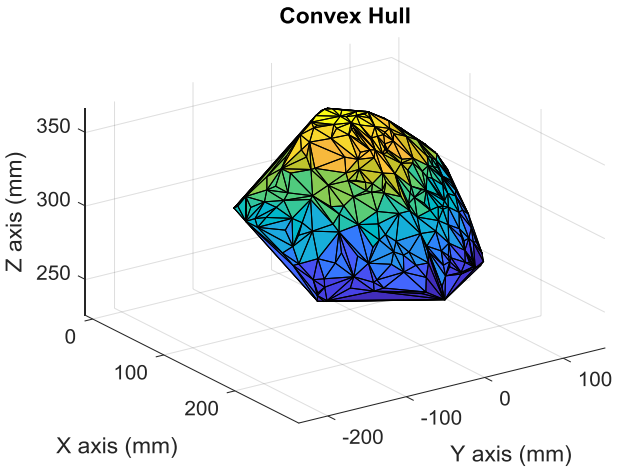

Figure 7. Surface wrap of the workspace for constant orientation at 0 °.

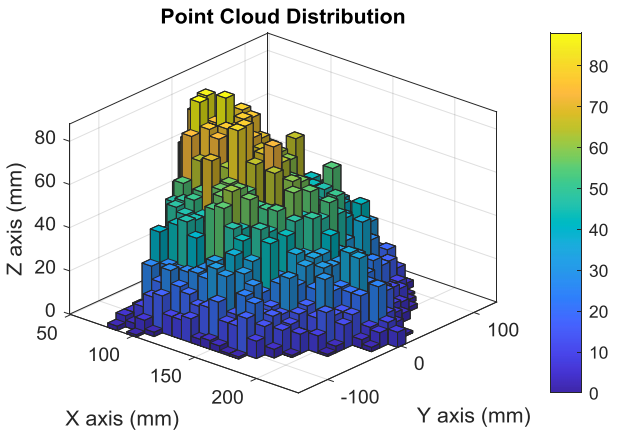

Figure 8. Point cloud distribution of 12000 points for constant orientation at 0 °.

Fig. 9 shows the point cloud workspace at various heights at constant orientation. The largest range of manipulation in the x and y directions is achieved between a height of 303 mm and 323 mm as highlighted by the planes containing both blue and red data points.

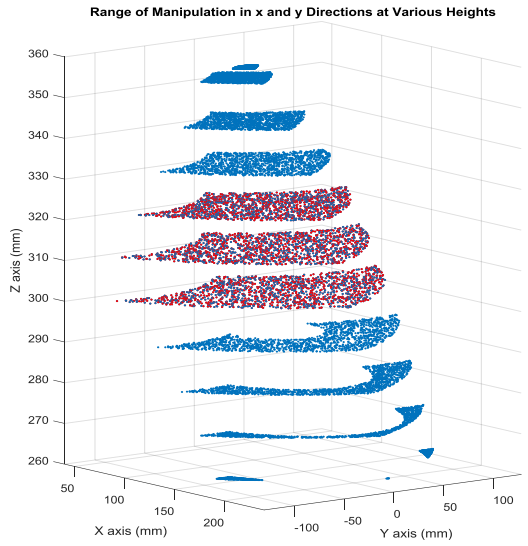

Figure 9. Isometric view of slices of the constant orientation workspace at different heights.

B. Inverse Kinematic Simulations

The aim of this test was to validate the inverse kinematic equations by comparing the values obtained from the virtual sensors in SolidWorks® to the values obtained from the kinematic calculations performed in MATLAB®. Inverse kinematic simulations were similarly conducted by researchers [24, 25].

The range of α and β rotations are 71.46 °and 63.97 ° respectively. The poses achieving the maximum positive and negative rotations are shown in Fig. 10. These values were obtained by moving the PKM to its extreme positions in SolidWorks® and measuring the rotation of the end effector.

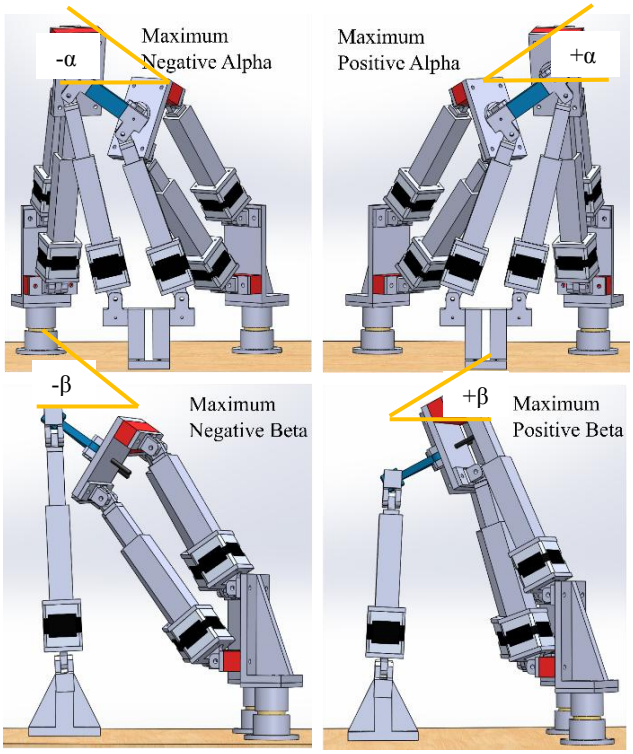

Figure 10. PKM postures for maximum positive and negative rotations.

Fifty random points were used for each case of translation, α rotation with translation and β rotation with translation. Therefore, one hundred and fifty random points were analysed across the workspace. The random points were selected across five different regions along the y axis as indicated in Table III and Fig. 11. This assisted the mitigation of a biased selection of coordinates.

TABLE III. SAMPLE REGIONS ALONG THE Y AXIS

Region	Range of y values (mm)
1	$-137.5 \leq y < -82.5$
2	$-82.5 \leq y < -27.5$
3	$-27.5 \leq y \leq 27.5$
4	$27.5 < y \leq 82.5$
5	$82.5 < y \leq 137.5$

The results of the inverse kinematic simulations are shown in Table IV. The inverse kinematic analysis exhibited high accuracy irrespective of the position and angle of tilt of the end effector. The errors observed from the inverse kinematic tests were attributed to truncation errors thus validating the inverse kinematic equations.

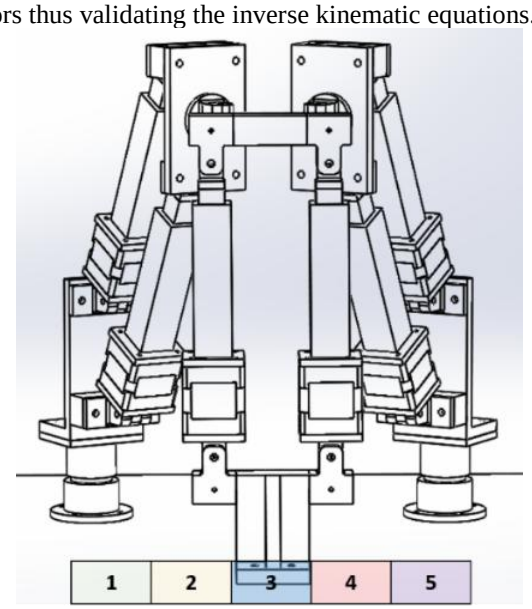

Figure 11. Regions of sample points equally spaced along the y axis.

TABLE IV. RESULTS OF THE INVERSE KINEMATIC SIMULATIONS

Variable	Minimum value from sample points	Maximum value from sample points
x (mm)	74.79	215.64
y (mm)	-137	125.08
z (mm)	269.26	336.95
α degrees	-27.33	31.34
β degrees	-25.19	20.18
Error statistics for limb lengths	Value	
Maximum (mm)	0.01	
Minimum (mm)	0	

V. Experimental Results

A. Accuracy and Repeatability Testing

The test aimed to determine the accuracy and repeatability of the PKM by measuring the position and orientation of the end effector. An Optical Computer Mouse (OCM) sensor was used in conjunction with MATLAB® as a low-cost displacement sensor to measure translational movement at a constant orientation of 0 °. Fig 12. shows the experimental scheme used for testing the translational movement at a constant orientation. The same approach was used when testing the rotation of the end effector but a Vernier caliper was used instead of OCMs. The experimental set-ups for measuring translation and rotation of the end effector is shown in Figs. 13–15.

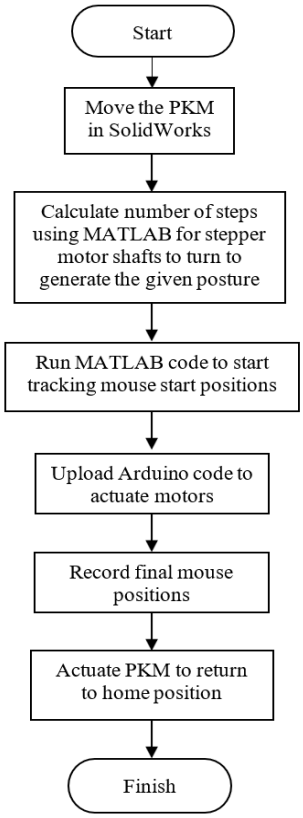

Figure 12. Accuracy and repeatability experimental scheme.

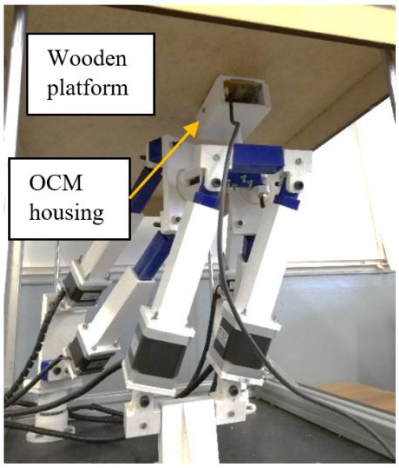

Figure 13. Accuracy and repeatability testing concerning translation.

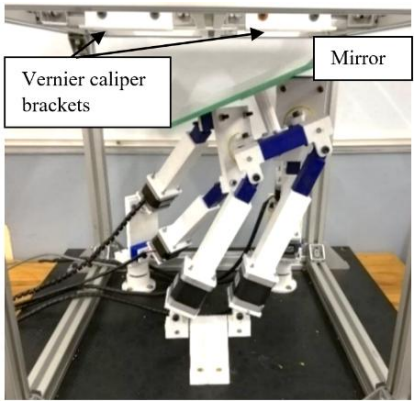

Figure 14. Accuracy and repeatability testing concerning rotation.

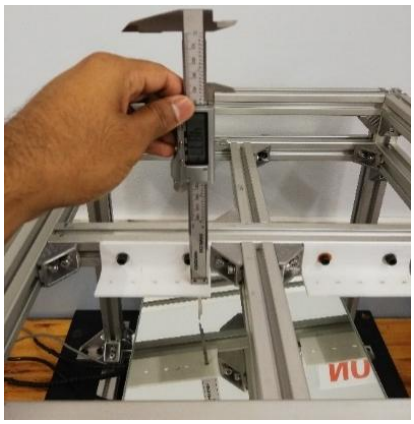

Figure 15. Measuring rotation with a Vernier caliper.

This research used the accuracy and repeatability formulae that are consistent with ISO 9283: 1998 and which were used by researchers [26–28]. Fifteen different points were used for each case of translation, α rotation with translation and β rotation with translation. The points were varied along the y axis by selecting 3 points from each region as detailed in Table III. The PKM was moved to each point ten times to obtain repeatability data. Concerning translation, the accuracy ranged from 1.17 mm to 1.91 mm and the repeatability ranged from 1.56 mm to 2.71 mm as shown in Fig. 16. Higher accuracies were observed for low y displacements indicating anisotropic behaviour concerning accuracy. The repeatability was low due to the high sensitivity of the OCM sensor and the tolerances observed from implementing additive manufactured joints which are not as tight and rigid as traditional metal joints.

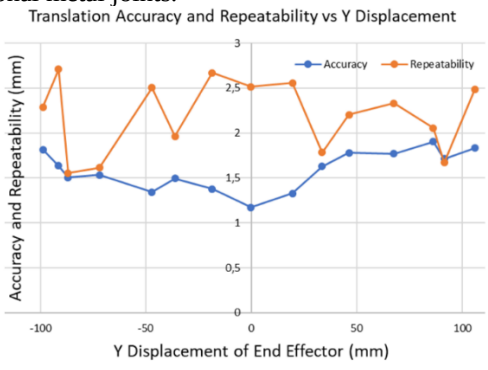

Figure 16. Graphs of accuracy and repeatability for translation.

When the end effector performed any rotation, translation could not be measured with the OCM sensor. The OCM loses surface contact and therefore loses functionality. The rotation of the end effector was measured using a digital Vernier caliper and the gradient formula. The digital Vernier caliper was placed on the brackets seen in Fig. 15. The brackets possessed holes with a predetermined spacing. The stem of the digital Vernier caliper was passed through a hole on the bracket until it reached the mirror. This process was repeated from another hole therefore providing a change in height. The change along the y axis was obtained from hole spacing on the brackets. The α rotation and translation yielded accuracies that ranged from 0.26 °to 1.74 °for the α angle. The repeatability ranged from 0.23 ° to 1.9 ° as shown in Fig. 17. For the β rotation and translation, the accuracy of the β angle ranged from 0.21 ° to 1.76 °. The repeatability ranged from 0.28 °to 1.33 °as shown in Fig. 18.

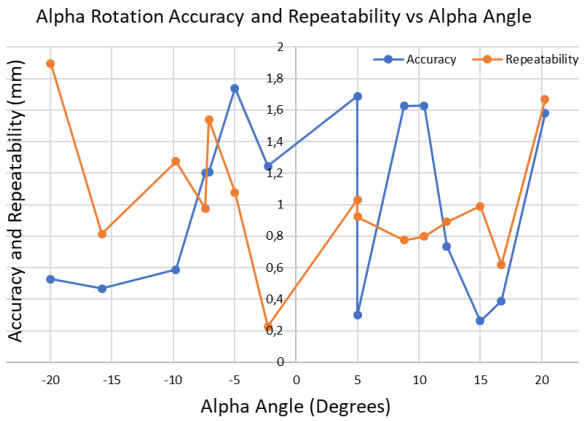

Figure 17. Graphs of accuracy and repeatability for α rotation with translation vs α angle.

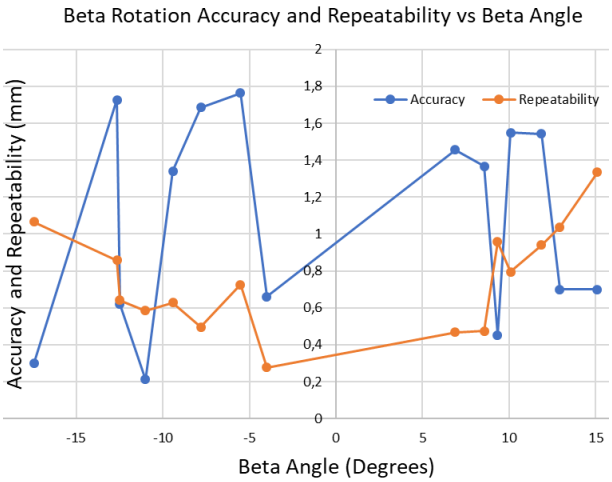

Figure 18. Graphs of accuracy and repeatability for β rotation with translation vs β angle.

VI. Conclusions

This research explored the use of actuated parallelogram joints and implemented exclusive use of single DOF joints. The traditional universal joints were substituted with orthogonal non-intersecting revolute joints. The aforementioned design considerations were used to develop a 5-DOF PKM which resulted in the generation of larger ranges of rotational motion. The tilt ranges achieved for α and β were 71.46 ° and 63.97 ° respectively. Although there are some PKMs that possess larger ranges of rotation, most of them possess fewer than 5 DOFs and many of these PKMs possess a hybrid structure. PKMs with 5-DOFs that possess larger ranges of rotation than the PKM in this study do not make use of only single DOF joints and do not possess actuated parallelogram joints. The decoupling of universal joints and actuated parallelogram joints created nested kinematic loops and required additional analytic consideration. The vector method was applied twice and successfully treated the implications mentioned.

The inverse kinematic simulations validated the application of the vector method and the equations that were developed only incurred errors due to truncation. The physical testing of the PKM concerning accuracy and repeatability produced acceptable results with errors originating from high sensor sensitivity and additive manufactured joints. The workspace of the PKM was generated using the Monte Carlo method and a convex hull boundary wrapping method.

The PKM in this research has further potential to exhibit tighter machine tolerances and high stiffness in comparison to other 5-DOF PKMs due the use of only single DOF joints. Future work includes investigation of the parasitic rotation, stiffness analysis, path planning, machine calibration, open architecture control, replacing additive manufactured joints with metal joints and implementation of high-quality sensors.

Conflict of Interest

The authors declare no conflict of interest.

Author Contributions

Wesley Dharmalingum conducted the research, performed the experiments and analyzed the data. Jared Padayachee supervised the research. All authors wrote the paper and revised the manuscript. All authors had approved the final version.

Funding

This research was supported by the University of KwaZulu-Natal and the National Research Foundation under the Thuthuka Grant (TTK170421228180).

References

[1] D. H. Salunkhe, G. Michel, S. Kumar, M. Sanguineti, and D. Chablat, "An efficient combined local and global search strategy for optimization of parallel kinematic mechanisms with joint limits and collision constraints," *Journal of Mechanism and Machine Theory*, vol. 173, Art. 104796, July 2022.

[2] Y. Patel, and P. George, "Parallel manipulators applications—a survey," *Journal of Modern Mechanical Engineering*, vol. 2, no. 3, pp. 57–64, Aug. 2012.

[3] X.-J. Liu, J. Wang, and G. Pritschow, "A new family of spatial 3-DoF fully-parallel manipulators with high rotational capability,"

Journal of Mechanism and Machine Theory, vol. 40, no. 4, pp. 475–494, Apr. 2005.
[4] M. M. Dalvand, B. Shirinzadeh, and S. Nahavandi, "Inverse kinematics Analysis of 6-RRCRR parallel manipulators," in *Proc. of the 2013 IEEE/ASME International Conf. on Advanced Intelligent Mechatronics*, 2013, pp. 644–648.
[5] Y. Yu, Z. B. Xu, Q. W. Wu, P. Yu, S. He, and G. Q. Wang, "Kinematic analysis and testing of a 6-RRRPRR parallel manipulator," in *Proc. of the Institution of Mechanical Engineers, Part C: Journal of Mechanical Engineering Science*, vol. 231, no. 13, pp. 2515–2527, July 2017.
[6] K. K. Oh, X. J. Liu, D. S. Kang, and J. Kim, "Optimal design of a micro parallel positioning platform. Part I: Kinematic analysis," *Journal of Robotica*, vol. 22, no. 6, pp. 599–609, Nov. 2004.
[7] K. K. Oh, X. J. Liu, D. S. Kang, and J. Kim, "Optimal design of a micro parallel positioning platform. Part II: Real machine design," *Journal of Robotica*, vol. 23, pp. 109–122, Jan. 2005.
[8] X. D. Jin, Y. F. Fang, S. Guo, and H.-B. Qu, "Structural synthesis of parallel mechanisms with high rotational capability," *Chinese Journal of Mechanical Engineering*, vol. 31, Art. 61, Dec. 2018.
[9] S. Staicu, Z. Shao, Z. Zhang, X. Tang, and L. Wang, "Kinematic analysis of the X4 translational–rotational parallel robot," *International Journal of Advanced Robotic Systems*, vol. 15, no. 5, pp. 1–12, Sept. 2018.
[10] X. Liu, Z. Xie, F. Xie, and J. Wang, "Design and development of a portable machining robot with parallel kinematics," in *Proc. of the 2019 16th International Conf. on Ubiquitous Robots (UR)*, 2019, pp. 133–136.
[11] Y. Xiaolong, L. Bin, and Z. Xinhua, "Kinematic analysis of a redundant actuated five degrees of freedom parallel mechanism," in *Proc. of the 2018 IEEE International Conf. on Robotics and Biomimetics (ROBIO)*, 2018, pp. 2031–2037.
[12] M. Weck and D. Staimer, "Parallel kinematic machine tools – current state and future potentials," *Journal of CIRP Annals*, vol. 51, no. 2, pp. 671–683, Jan. 2002.
[13] T. Sun, B. Lian, Y. Song, and L. Feng, "Elastodynamic optimization of a 5-dof parallel kinematic machine considering parameter uncertainty," *Journal of IEEE/ASME Transactions on Mechatronics*, vol. 24, no. 1, pp. 315–325, Feb. 2019.
[14] Z. Pandilov, and V. Dukovski, "Comparison of the characteristics between serial and parallel robots," *Journal of Acta Technica Corviniensis-Bulletin of Engineering*, vol. 7, no. 1, pp. 143–160, Jan. 2014.
[15] S.V. Kiselev, A.V. Antonov, and A.S. Fomin, "Parallel robots with a circular guide: systematic review of kinematic schemes and methods of synthesis and analysis," *Journal of Machinery Manufacture and Reliability*, vol. 51, no. 1, pp. 20–29, Feb. 2022.
[16] M. Qazani, S. Pedrammehr, A. Rahmani, B. Danaei, M. Ettefagh, A. Rajab, and H. Abdi, "Kinematic analysis and workspace determination of hexarot-a novel 6-DOF parallel manipulator with a rotation-symmetric arm system," *Journal of Robotica*, vol. 33, no. 8, pp. 1686–1703, Oct. 2015.
[17] C. Gosselin, T. Laliberté, and A. Veillette, "Singularity-Free Kinematically Redundant Planar Parallel Mechanisms with Unlimited Rotational Capability," *Journal of IEEE Transactions on Robotics*, vol. 31, no. 2, pp. 457–467, Apr. 2015.
[18] L. -T. Schreiber, and C. Gosselin, "Schönflies motion parallel robot (spara): A kinematically redundant parallel robot with unlimited rotation capabilities," *Journal of IEEE/ASME Transactions on Mechatronics*, vol. 24, no. 5, pp. 2273–2281, Oct. 2019.
[19] J.-P. Merlet, *Parallel Robots*, 2nd ed. Dordrecht, Netherlands: Springer, 2006, ch. 1, pp. 13–17.
[20] S. Briot, and W. Khalil, *Dynamics of Parallel Robots: From Rigid Bodies to Flexible Elements.* 1st ed. Switzerland: Springer Cham, 2015, ch. 1, pp. 13–14.
[21] A. Chaudhury and A. Ghosal, "Determination of workspace volume of parallel manipulators using monte carlo method," in *Proc. Computational Kinematics. Mechanisms and Machine Science*, vol. 50, S. Zeghloul, L. Romdhane, M. Laribi, Ed. Cham, Springer, 2018, pp. 323–330.
[22] E. Kuznetcova, V. Titov, E. Smirnov, I. Dalyaev, and A. Truts, "Design and Simulation Analysis of Haptic Device with Parallel Kinematics," in *Proc. 2018 29th DAAAM International Symposium*, B. Katalinic, Ed. Vienna: DAAAM International, 2018, pp. 0636–0644.
[23] Y. Cao, K. Lu, X. Li, and Y. Zang, "Accurate numerical methods for computing 2d and 3d robot workspace," *International Journal of Advanced Robotic Systems*, vol. 8, no. 6, pp. 76–88, Dec. 2011.
[24] W. Xu, Y. Li, and X. Xiao, "Kinematics and workspace analysis for a novel 6-PSS parallel manipulator," in *Proc. 2013 IEEE International Conf. on Robotics and Biomimetics (ROBIO)*, Shenzhen, 2013, pp. 1869–1874.
[25] Y. Zhang, and X. Jing, "Kinematics analysis and simulation of a novel spatial translational parallel manipulator," in *Proc 2017 2nd International Conf. on Robotics and Automation Engineering*, 2017, pp. 131–135.
[26] L. Zhao, A. Joubair, P. Bigras, and I. A. Bonev, "Metrological evaluation of a novel medical robot and its kinematic calibration," *International Journal of Advanced Robotic Systems*, vol. 12, no. 9, pp. 126–138, Sept. 2015.
[27] M. PłAczek and Ł. Piszczek, "Testing of an industrial robot's accuracy and repeatability in off and online environment," *Journal of Maintenance and Reliability*, vol. 20, no.3, pp. 455–464, Sept. 2018.
[28] D. Kumičáková, V. Tlach, and M. Císar, "Testing the performance characteristics of manipulating industrial robots," *Transactions of the VŠB - Technical University of Ostrava, Mechanical Series*, vol. 62, no. 1, pp. 39–50, Sept. 2016.